Flow in the Lee of Idealized Mountains and Greenland

GUÐÚN NÍNA PETERSEN

University of Oslo, Oslo, Norway, and University of Iceland, Reykjavik, Iceland

HARALDUR ÓLAFSSON

University of Iceland, Icelandic Meteorological Institute, and Institute for Meteorological Research, Reykjavik, Iceland

JÓN EGILL KRISTJÁNSSON

University of Oslo, Oslo, Norway

(Manuscript received 7 January 2002, in final form 24 March 2003)

ABSTRACT

A series of idealized simulations of flow impinging on large mountains is conducted to investigate the impact of the mountain on the flow far downstream and to shed some light on the effects that Greenland may have on airflow over the North Atlantic. The upstream profiles of wind and stability are kept constant, there is no surface friction, the Rossby number is 0.4, and the nondimensional mountain height ($\hat{h} = Nh/U$) is varied from 1 to 6. The maximum sea level pressure deficit, the maximum geopotential height deficit, and the orographically generated potential vorticity all increase with increased $\hat{h}$, showing no signs of abrupt change as the flow enters the regime of upstream blocking. The potential vorticity produced at the mountain is accumulated in vortices that are advected downstream. The vortices are associated with a larger pressure gradient to the south of the wake, giving rise to stronger westerlies at the surface as well as at upper levels.

This process can explain how Greenland may affect cyclones moving far outside the mountain wake. An example from Fronts and Atlantic Storm Track Experiment (FASTEX) shows that a cyclone moving from the southwest toward Scotland becomes shallower and slower if the Greenland topography is removed.

1. Introduction

Orographic effects on atmospheric flow have been investigated by numerous authors, ranging from the analytical models of two-dimensional linear mountain waves by Queney (1948) and Eliassen and Palm (1960) to studies in three dimensions and of nonlinear vertically structured flow (e.g., Smith 1989; Duran 1990; Grubišić et al. 1995; Ólafsson and Bougeault 1996, 1997; Epifanio and Durran 2001).

Extensive work has been done on large mountain ridges like the Rocky Mountains (e.g., Steenburgh and Mass 1994; Davis 1997), the Alps (e.g., Thorpe et al. 1993; Aebisher and Schär 1998) and the Pyrenees (Bougeault et al. 1997). On the other hand, little research has been done on the impact of Greenland on atmospheric flow. Cyclonic developments in the vicinity of Greenland and Iceland are often poorly captured by NWP models (Ólafsson 1998), which cannot only have a large impact over Iceland in short-range forecasts, but also over continental Europe some days later. The Icelandic low is a well-known climate feature, particularly during wintertime due to great cyclone activity in the vicinity of Iceland. It has been suggested that the low owes its existence partly to thermal forcing, and this has, in fact, been confirmed by numerical simulations using a global circulation model (Held 1983), where, in the absence of topography, the Icelandic low still appears. However, it is also reasonable to believe that the orography of Greenland may play an important role in explaining the position and persistence of the low. Harold et al. (1999a,b) studied meso- and synoptic-scale cyclones observed on satellite images over the northeast Atlantic and Nordic Seas during a 2-yr period. They noted that 58% of the cyclones found just east of south Greenland formed and decayed in the area. Furthermore, the finding of a relatively frequent occurrence of cyclones with a diameter of 200–600 km in the same area, suggests lee cyclone development. Kristjánsson and McInnes (1999) did a case study of Greenland's impact on cyclone activity in the North Atlantic and found evidence that the deepening of a baroclinic cyclone near Iceland was hampered by the presence of Greenland's orography and the development of a residual low be-

Corresponding author address: Guðún Nína Petersen, Department of Geophysics, University of Oslo, Pb 1022 Blindern, 0315 Oslo, Norway.
E-mail: gnp@geofysikk.uio.no

© 2003 American Meteorological Society

tween Greenland and Iceland was induced. Breivik et al. (1992) found, in their investigation of the 1 January 1992 explosive cyclone (Grønås 1995), that Greenland's orography had a large impact on the cyclone's track and strength. They suggested that Greenland strongly affects the large-scale vorticity budget by creating a quasi-stationary lee cyclone between Greenland and Iceland as well as having an impact on the advection of arctic air towards the cyclone. Doyle and Shapiro (1999) investigated the Greenland tip jet, defining a tip jet as the narrow low-level jet stream originating from the vertex of large elliptical barriers. They found the strength of the tip jet to be most sensitive to changes in the nondimensional mountain height and the Rossby number, emphasizing the importance of the orographic deflection of airflows and acceleration on the downstream slope.

The aim of this study is to obtain a better understanding of Greenland's impact on the airflow over the North Atlantic. One approach is to start with idealized simulations. A series of simulations of three-dimensional flow over an elliptical mountain on a rotating plane are conducted. The mountain has approximately the same half-width and half-length as Greenland, especially the southern part of Greenland, but the height is varied. The idealized flows have uniform upstream vertical profile of wind and stability. Subsequently, a case study of flow in the vicinity of Greenland is described and discussed in the light of the idealized simulations.

In the following section there is a short overview of the theory of simple flow, followed by a description of the numerical model and the parameters used in the idealized simulations in section 3. The idealized simulations are described in section 4 and the case study in section 5. Finally, a discussion and conclusions are given in section 6.

2. Theory

Two of the key features of stratified flow past obstacles are upstream blocking and wake (e.g., Smolarkiewicz and Rotunno 1990; Smith et al. 1997). Ólafsson and Bougeault (1996) defined upstream blocking as a mass of decelerated air upstream with a partly reversed flow. Another way to define the blocking is by one or more stagnation points on the windward slope, followed by flow splitting. This definition will be applied in this paper. Rotunno et al. (1999) defined a wake as a region of decelerated air mass downstream of an obstacle and possibly reversed flow. In some of the simulations presented is this study, the flow in the lee of the mountain is highly unstable with vortex shedding downstream making it difficult to characterize the flow as decelerated. The term wake is here, therefore, defined as a region downstream of an obstacle where the air is decelerated or there is eddy shedding.

A hydrostatic, frictionless, Boussinesq flow on a nonrotating plane is governed by the mountain shape, its aspect ratio $r = L_y/L_x$; its nondimensional mountain height, $\hat{h} = Nh/U$; and the profile of the atmosphere (Smith and Grønås 1993). Here L_y and L_x are the mountain half-length and half-width, respectively, N is upstream Brunt–Väisälä frequency, h the mountain height, and U the upstream wind speed.

According to Smith (1989), a linear, hydrostatic, frictionless, stratified flow over a mountain on a nonrotating plane can be divided into three main categories: (a) for small $\hat{h}$, the low-level flow is able to climb the mountain and smooth mountain waves are created above the mountain; (b) for large $\hat{h}$ and $r < 1$, a stagnation point forms on the windward side of the mountain and the flow splits; and (c) for large $\hat{h}$ and $r > 1$, a stagnation point forms aloft leading to wave breaking. For even larger $\hat{h}$, the flow in the last category will, in addition, experience flow splitting.

Ólafsson and Bougeault (1996) showed that nonlinear irrotational inviscid flow past an elongated mountain was in agreement with Smith's diagram. They also showed that increasing $\hat{h}$ even further results in wave breaking that is no longer on the axis of symmetry, but is in isolated areas on each side of the axis.

When the Coriolis force is included, the Rossby number enters as an additional parameter and the morphology of the flow changes. The left–right symmetry of the flow is broken and the flow is to a greater extent diverted to the left (facing downstream), giving greater wind speed than on the right side of the mountain (Pierrehumbert and Wyman 1985) and delaying the onset of upstream blocking (Thorsteinsson and Sigurðsson 1996). Ólafsson and Bougeault (1997) studied the effect of rotation and surface friction on orographic drag and found that when the flow is blocked there is a permanent downward deflection of the isentropes in the lee. The pressure deficit in the lee is reduced by the Coriolis force, while surface friction acts more to modify the structure of the wake, by suppressing wave activity and bringing the orographic drag closer to its linear value (Ólafsson and Bourgeault, their Fig. 7). Ólafsson (2000) noticed that when rotation and friction are included, stagnation aloft does not occur, the flow is then simply either blocked or not blocked, depending on the nondimensional mountain height, the aspect ratio, the Rossby number and the Reynolds number.

Smolarkiewicz and Rotunno (1989) established that it is possible for vortices to form in continuous stratified flow past isolated mountains in the absence of surface friction. Schär and Smith (1993), Schär (1993), and Schär and Durran (1997) stressed that when neglecting surface friction, internal dissipation, and diffusion are the only factors available to reduce the value of the Bernoulli function and hence generate potential vorticity (PV) anomalies that are associated with the wake. The PV value can either be reduced by strong and concentrated dissipation in the wave breaking area over the mountain or by weak and widespread dissipation in the recirculating wake. Rotunno et al. (1999) argued that the vertical vorticity must be produced through the tilt-

ing of baroclinically generated horizontal vorticity, and that dissipation enters indirectly through its effect on the tilting term. Epifanio and Durran (2002) confirmed the baroclinic generation, but emphasized that the vertical vorticity produced is relatively weak. A vertical stretching in a hydraulic jumplike feature in the lee is necessary to amplify the vorticity significantly and produce the pronounced vertical vorticity anomaly. The PV generation in the jump is then primarily generated through thermal diffusion tending to modify the potential temperature field following the flow so as to produce PV from the vertical vorticity present in the jump.

3. The experimental setup

The third version of the fifth-generation Pennsylvania State University–National Center for Atmospheric Research (PSU–NCAR) Mesoscale Model (MM5) is used in this study (Grell et al. 1995). It is a nonhydrostatic sigma-coordinate model designed to simulate or predict mesoscale and regional-scale circulations. It has been used for a broad spectrum of theoretical as well as real-time studies.

A second-order leapfrog time step scheme is applied, but some terms in the basic equations are handled using a time splitting scheme. The time step in the experiments is 90 s.

The horizontal grid has an Arakawa–Lamb B-staggering of the velocity variables with respect to the scalars. The idealized experiments presented here have all been run with a 36-km horizontal grid resolution and 150 $\times$ 150 grid points in the horizontal. In the vertical there are 40 σ levels, where the σ coordinate is defined by

$$\sigma = \frac{p - p_t}{p_s - p_t}. \tag{1}$$

Here, p is the pressure, p_t is a specified constant top pressure (10 hPa), and p_s is the surface pressure. To prevent wave reflection, a Rayleigh damping layer, which is not a standard parameterization in MM5, is included. The layer is placed above 13-km height and the wave absorption coefficient increases with height, according to Klemp and Lilly (1978). In the simulations the atmosphere is simple, neither humidity nor radiation are included. The horizontal diffusion in MM5 is done by a common horizontal diffusion scheme while the PBL schemes compute the vertical mixing. High concentration of turbulent kinetic energy, together with steep isentropes, is a major criterion for the detection of wave breaking as in Ólafsson and Bougeault (1996). Thus from the PBL schemes available, a PBL scheme (Burk and Thompson 1989) that predicts turbulent kinetic energy for use in vertical mixing, based on the Mellor–Yamada formulas (Mellor and Yamada 1982), was chosen. The turbulent fluxes at the lowest σ level were set to zero, to enable the use of free slip at the lower boundary.

The mountain in the experiments with idealized flows is bell shaped and given by the equation

$$H(x, y) = \frac{h}{[1 + (x/L_x)^2 + (y/L_y)^2]^{1.5}}, \tag{2}$$

where h is the mountain height and L_x and L_y are the mountain half-width and half-length, respectively. Here, we set L_x to 200 km and L_y to 800 km, giving an aspect ratio $r = L_y/L_x = 4$.

The nondimensional mountain height, $\hat{h} = Nh/U$, is often referred to as the inverse Froude number. In most of the simulations the model was initialized everywhere with $U = 10$ m s^{-1} and $N = 0.01$ s^{-1}. The nondimensional mountain height is then varied by changing the mountain height. Thus, a high $\hat{h}$ represents a high mountain. Also, because the half-length and half-width of the mountain are held constant, a higher mountain is steeper than a lower mountain. The Coriolis parameter f was set to 1.2×10^{-4} s^{-1}, which is a value representative for about 55°N. The Rossby number, Ro $= U/fL_x$, is 0.42.

Simple idealized flow past a smooth analytic mountain such as used in this study is governed by three parameters, the nondimensional mountain height $\hat{h}$, the Rossby number Ro, and the aspect ratio r. When exploring the effect of $\hat{h}$ it is essential that the other two remain constant. In other words, if $\hat{h}$ is changed through U, the combination of U, f, and L_x in the Rossby number must also change. Furthermore, a change in Ro through L_x necessitates a change in L_y for the aspect ratio to remain constant and such a change is not suitable for this study, which is focused on mountains of Greenland's size.

A series of simulations was done with different combinations of N, h, and U, keeping the same $\hat{h}$ and a constant Rossby number. Table 1 summarizes the values of each of these parameters in the simulations. The name of each simulation contains the value of $\hat{h}$. The experiments that have been given a name with a ''D'' at the end represent a different combination of N and h than mentioned earlier, and the experiments with upstream velocity not equal to 10 m s^{-1} have a ''U'' followed by the velocity. A simulation with the idealized mountain replaced by Greenland is termed exgreen.

A number of normalizations were tried out for the three parameters studied in this paper—sea level pressure perturbations and geopotential height perturbations at the 500-hPa level, both calculated in the wake, and mean potential vorticity in a small subdomain downstream of the mountain. The normalizations applied in this study are as follows: The sea level pressure perturbations are normalized with $\rho_o UfL_x$, where ρ_o is a constant density and U upstream velocity. The geopotential height perturbations at the 500-hPa level are normalized with the vertical wavelength, U/N. The mean potential vorticity is normalized with $\theta_o N/\rho_o h$, where θ_o and ρ_o are constants but N and h vary between simulations.

TABLE 1. An overview of the simulations. The name of each experiment includes the value of the nondimensional mountain height ($\hat{h} = Nh/U$), a D if the combination of N and h is different from the one mentioned in the text, and a U followed by the upstream wind speed if U has a different value than mentioned in the text.

Expt	Mountain height (m)	Brunt–Väisäla frequency (s^{-1})	Upstream wind ($m\ s^{-1}$)	Coriolis parameter ($10^{-4}\ s^{-1}$)	$\hat{h}=NH/U$
ex10	1000	0.01	10	1.2	1.0
ex10D	2000	0.005	10	1.2	1.0
ex15	1500	0.01	10	1.2	1.5
ex15D	2000	0.0075	10	1.2	1.5
ex20	2000	0.01	10	1.2	2.0
ex20D	2500	0.008	10	1.2	2.0
ex20U18	3000	0.012	18	2.16	2.0
ex25	2500	0.01	10	1.2	2.5
ex25D	2000	0.0125	10	1.2	2.5
ex30	3000	0.01	10	1.2	3.0
ex30D	2000	0.015	10	1.2	3.0
ex30U12	3600	0.01	12	1.44	3.0
ex30U15	3000	0.015	15	1.8	3.0
ex30U20	5000	0.012	20	2.4	3.0
ex35	3500	0.01	10	1.2	3.5
ex35D	2500	0.014	10	1.2	3.5
ex40	4000	0.01	10	1.2	4.0
ex40D	2500	0.016	10	1.2	4.0
ex40U8	3200	0.01	8	0.96	4.0
ex45	4500	0.01	10	1.2	4.5
ex45D	2500	0.018	10	1.2	4.5
ex60	6000	0.01	10	1.2	6.0
ex60D	3750	0.016	10	1.2	6.0
exgreen	3199	0.01	10	1.2	3.2

The model was run for 336 h or 60.48 nondimensional time units ($t^* = Ut/L_x$) in all the simulations except one, which was run for a shorter time period. The initial perturbation has been advected out of the domain after about $t^* \approx 34$ and with the long simulation time it is quite easy to classify the flows as quasi-stationary flows or highly unstable flows. Due to this dependency on the initial condition the time means calculated in the study are means from $t^* = 34.56$, with the time interval $t^* = 1.08$, until the end of the simulations.

4. Simple idealized flows

a. Idealized flows past a smooth mountain

The simulations in this study were conducted with a nonhydrostatic, nonlinear weather prediction model, on a rotating plane, with a free-slip condition at the lower boundary. In order to investigate if the model is able to reproduce the $\hat{h}$ similarity expected on a nonrotating plane, two simulations with the same $\hat{h}$ but different combinations of N and h were conducted, excluding the Coriolis force. They were compared and good similarity was found in sea level pressure deficit and geopotential height deficit at 500 hPa. Simulations with five different $\hat{h}$ were compared to Smith's diagram, with the extension of Ólafsson and Bougeault (1996), and the flow pattern found to be in agreement with the diagram.

The delay of the onset of blocking, due to the Coriolis force is seen clearly when comparing simulations with the same $\hat{h}$, one including the Coriolis force, Ro = 0.42, and the other excluding it, Ro = ∞. Figure 1 shows such a comparison for $\hat{h} = 1.5$. In the absence of rotation, the flow experiences wave breaking and upstream blocking, as can be seen from the steep isentropes, the high concentration of turbulent kinetic energy (TKE) and the upstream stagnation point. When the Coriolis force is included, only wave breaking occurs and it is less pronounced and in a smaller region.

Figure 2 shows the sea level pressure for different values of $\hat{h}$ at $t^* = 43.2$, where sea level pressure is the pressure field at the lowest model terrain-following surface extrapolated down to the elevation of 0 m. Upstream of the mountain the isobars are deflected to the left. In the lee of the mountain there is a pressure deficit extending far downstream for low $\hat{h}$ but for high $\hat{h}$ there are large variations in the pressure field. For $\hat{h}$ less than or equal to 2, the flow is unblocked and reaches quasi stationarity after about 34 nondimensional time units; while for larger $\hat{h}$, vortices are shed downstream from the mountain. In the case of $\hat{h}$ equal to 2.5 and 3, the flow is unblocked, the vortex shedding decreases with time, and the vortices appear farther away from the mountain during the simulation. By the end of the simulations the flow near the mountain shows little variation in time, and it is therefore expected that the flow will reach quasi stationarity, given sufficient time. In the simulations with $\hat{h}$ greater than 3, the flow is blocked and nonstationary. Vortices are formed continuously on the northern side of the tip jet and there is continuous vortex shedding in the wake. The downstream pressure

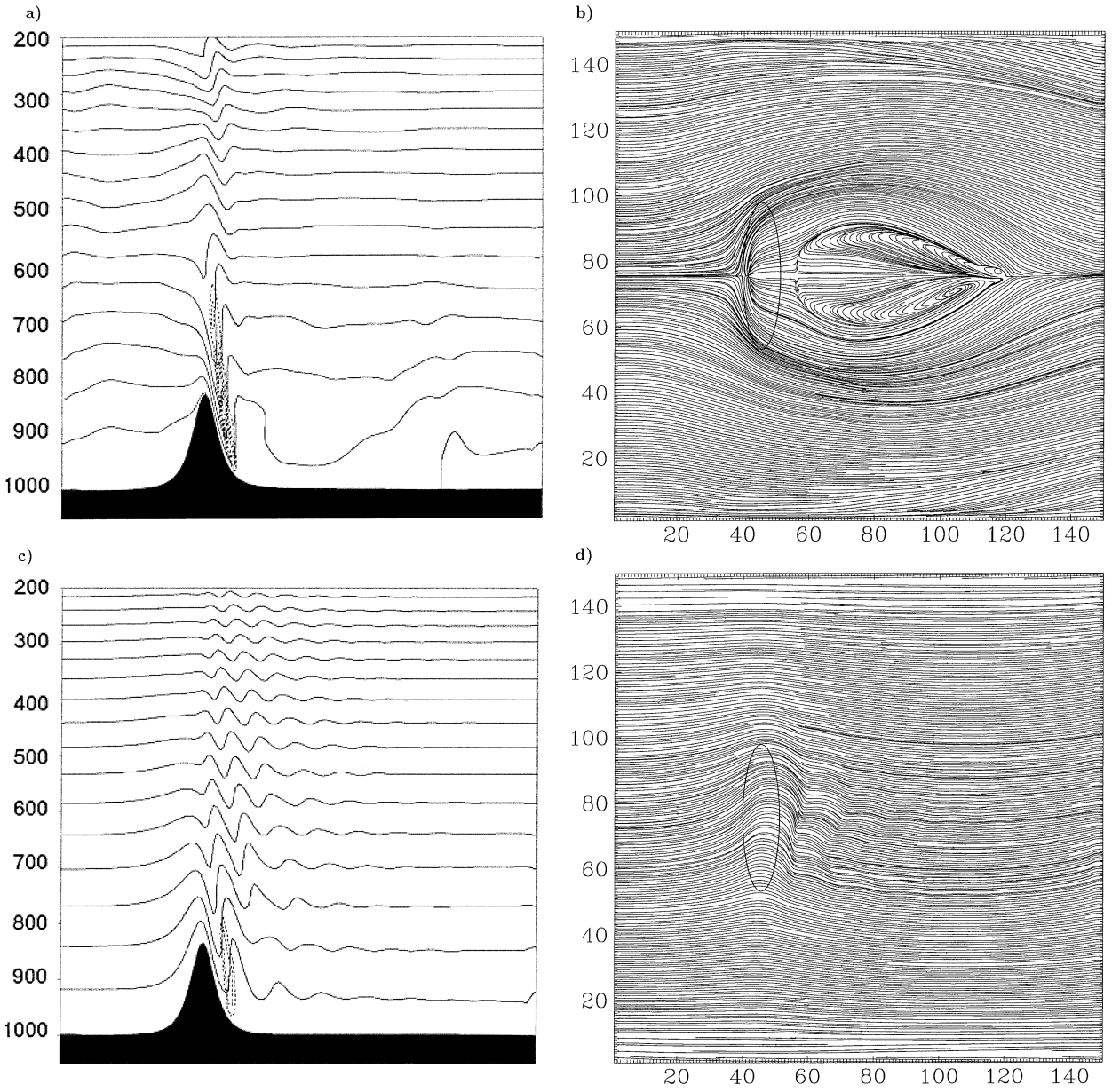

FIG. 1. Comparison of simulations excluding and including the Coriolis force. (a) A cross section of a flow with $\hat{h} = 1.5$ and Ro $= \infty$, taken at the axis of symmetry at $t^* = 34.56$ showing potential temperature (K, solid) and turbulent kinetic energy (J kg^{-1}, dashed). The isentrope contour interval is 2 K and the TKE contour interval 1 J kg^{-1}. (b) Streamlines at the surface at the same time. The topography is shown at 0.35h. (c), (d) As in (a), (b) but with Ro $= 0.42$.

field varies greatly in time, depending on whether the flow is dominated by a high pressure ridge or a low.

The time evolution can be further investigated in Fig. 3. The figure shows the evolution of the normalized maximum pressure deficit at sea level downstream of the mountain. The curves have local minima when a low is dominating the flow in the lee, and maxima when a high pressure ridge is dominating. The pressure perturbations increase with $\hat{h}$ and so does the difference between the minimum and the maximum perturbation. Also, for the nonstationary flows there seems to be a lag of the maximum value as $\hat{h}$ increases. In the simulations with $\hat{h}$ less than 2.5, the flow has reached stationarity at $t^* = 34.56$, but in the case of ex25 the perturbations do not reach a constant value until $t^* = 47.52$ (equal to 264 h of simulation). Figure 4 shows the time evolution of the normalized maximum deficit of the geopotential height at the 500-hPa level. The results are similar to the ones for the sea level pressure perturbations.

When the Coriolis force is included in the equations, the Rossby number is added to the governing nondi-

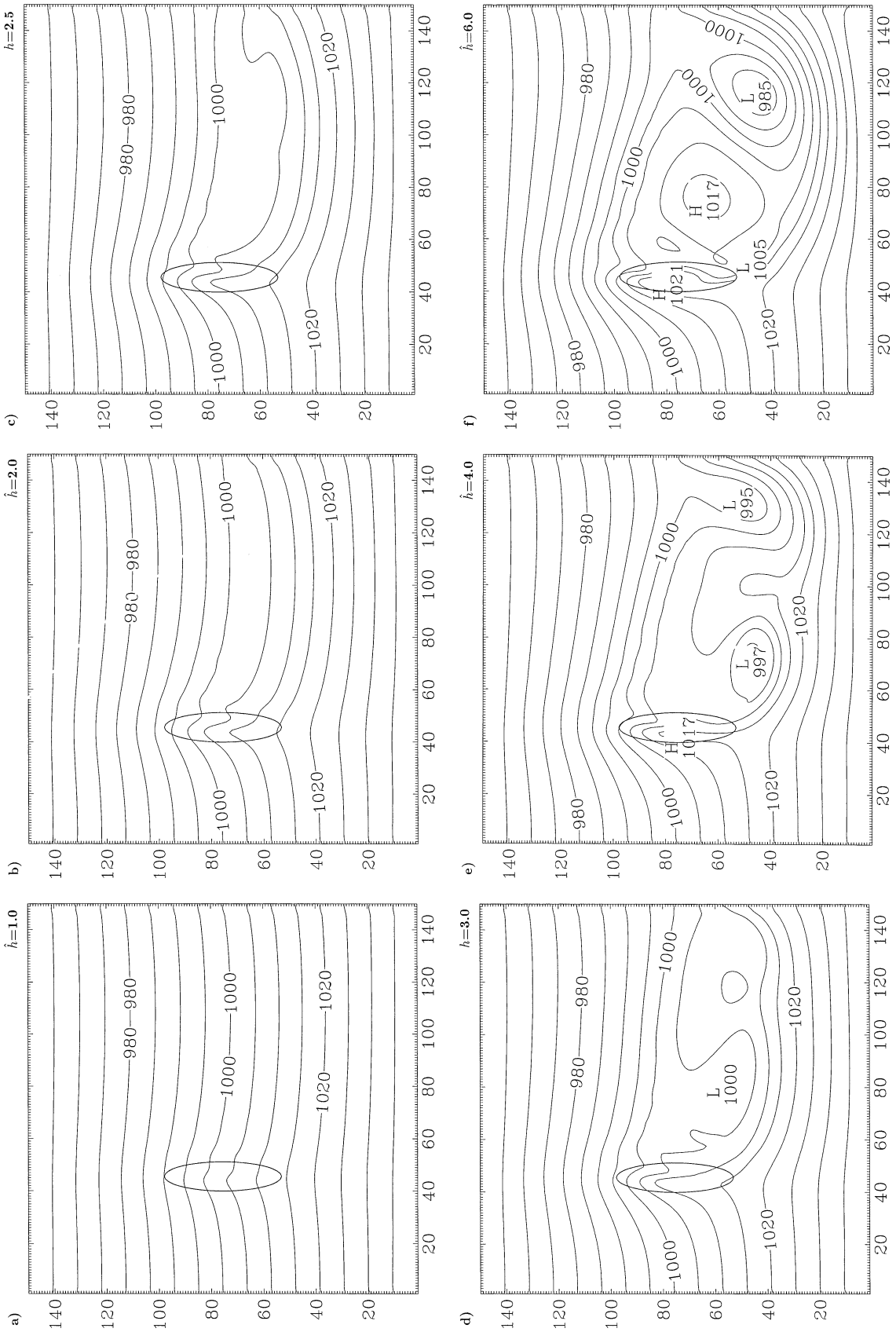

FIG. 2. The sea level pressure (hPa) for different values of $\hat{h}$, with $r = 4$ and Ro = 0.42, at $t^* = 43.2$. (a)–(f) Values of $\hat{h}$ at upper-right corner. Topography at $0.35h$.

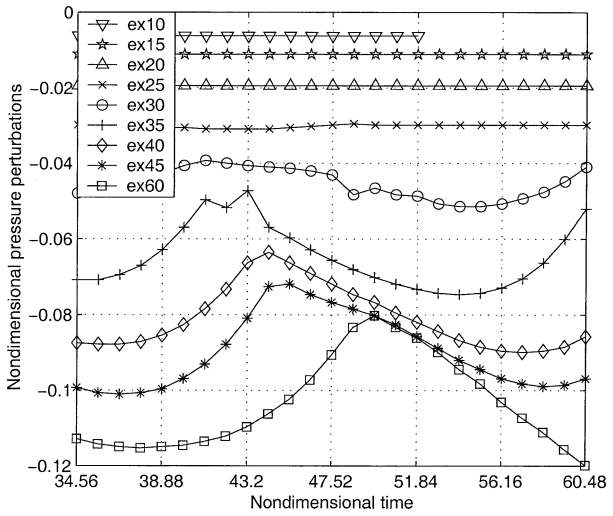

FIG. 3. The time evolution of the nondimensional max sea level pressure deficit downstream of the mountain for different $\hat{h}$. The value at each time step is normalized by $\rho_o UfL_x$, where $\rho_o = 1.2$ kg m^{-3}.

mensional numbers. To test the $\hat{h}$ similarity, the flow is simulated with different values of N, h, and U, giving the same $\hat{h}$ as before. The time means of the maximum perturbations are shown in Figs. 5 and 6. The figures show little sensitivity to the combination of N and h, confirming an $\hat{h}$ similarity on a rotating plane for a constant U (10 m s^{-1}), and even for a varied U in the case of sea level pressure. The similarity is, on the other hand, poor for the 500-hPa geopotential height when U is varied. The simulations show that for $U = 10$ m s^{-1} the magnitude of the perturbations increases by a factor of 5 as $\hat{h}$ increases from 2 to 6. Interestingly, even though the increase with $\hat{h}$ is strongest at the regime

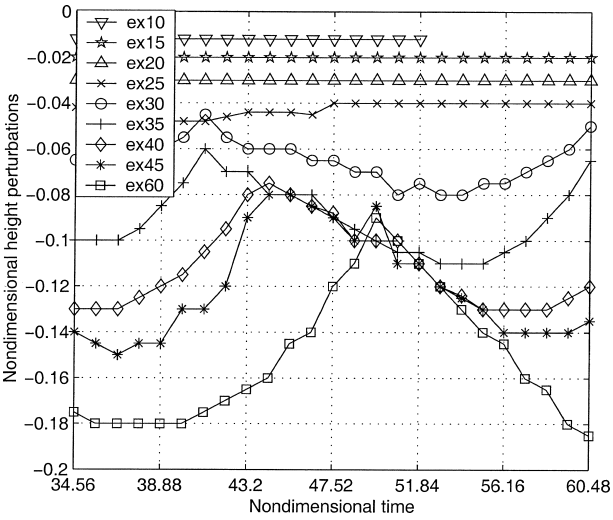

FIG. 4. The time evolution of the nondimensional max deficit in the geopotential height at 500 hPa downstream of the mountain for different $\hat{h}$. The value at each time step is normalized by the vertical wavelength, U/N.

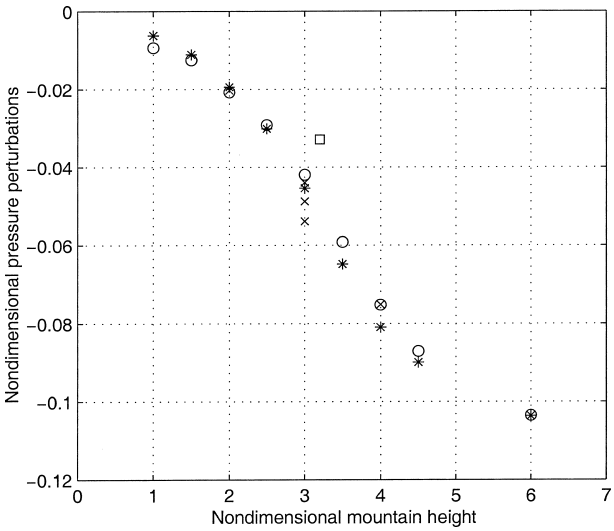

FIG. 5. Nondimensional max sea level pressure deficit downstream of the mountain as a function of $\hat{h}$. The perturbations are normalized by $\rho_o UfL_x$, where $\rho_o = 1.2$ kg m^{-3}. Simulations with $N = 0.01$ s^{-1} and $U = 10$ m s^{-1} (stars), with different combinations of N and h (circles), and where U was varied (crosses) (see Table 1). The exgreen simulation (square).

shift between unblocked and blocked flow, no abrupt change is found in the perturbations at the regime shift.

As the flow is undisturbed far to the south of the mountain the geopotential height deficit in the lee of the mountain results in an enhanced geopotential gradient in the area between these two regions. Figure 7 shows the maximum westerly wind component in this area as a function of $\hat{h}$ and the distance from the mountain

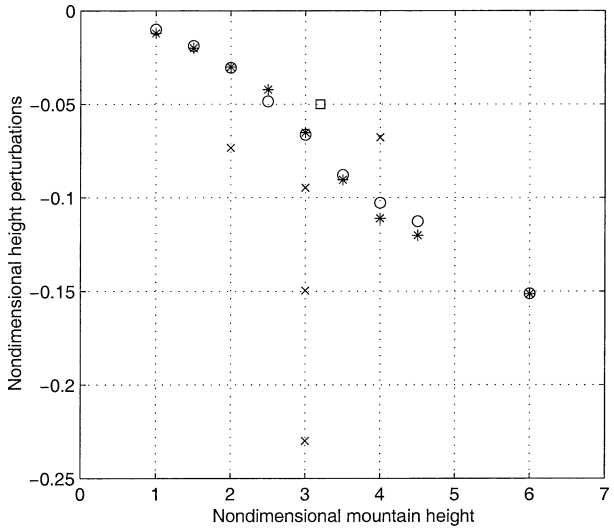

FIG. 6. Nondimensional max height deficit at 500 hPa downstream of the mountain as a function of $\hat{h}$. The perturbations are normalized by the upstream vertical wavelength, U/N. Simulations with $N = 0.01$ s^{-1} and $U = 10$ m s^{-1} (stars), with different combinations of N and h (circles), and where U was varied (crosses) (see Table 1). The exgreen simulation (square).

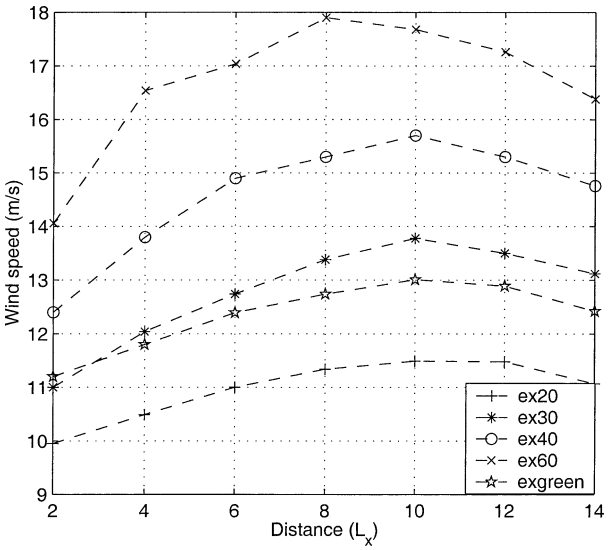

FIG. 7. Maximum westerly wind component (m s^{-1}) at 500-hPa level downstream of the mountain as a function of $\hat{h}$ and the mountain half-widths from the mountain centerline.

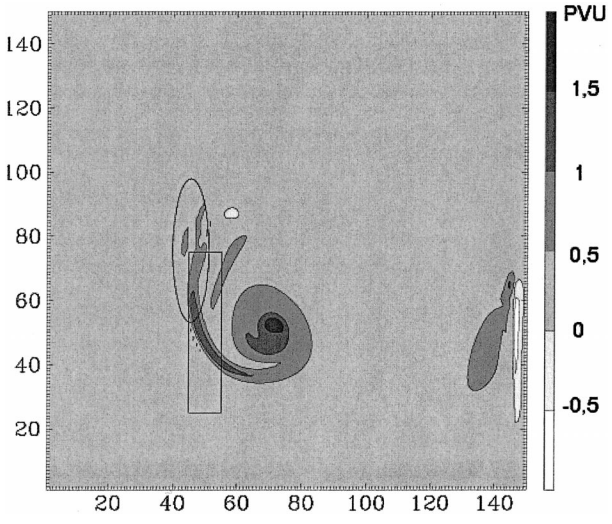

FIG. 8. Potential vorticity (PV) at $\sigma = 0.943$ in ex60, $t^* = 51.84$. The rectangle shows the horizontal area of the box for which the potential vorticity is integrated over. Mountain height at 0.35h.

center line. The figure shows an increase in the wind speed as $\hat{h}$ increases but note also that the greatest velocity is not in the area nearest to the mountain but about 10 half-widths downstream.

Due to its applications in atmospheric research the potential vorticity of the flow was investigated. In addition to the potential vorticity produced by the mountain by internal dissipation, the simulations all have background potential vorticity due to the Coriolis force; see Fig. 8. The figure also shows a PV banner emerging from the mountain, reaching out to a low southeast of the mountain where there is a PV maximum. Downstream, at the end of the domain, there is some PV related to a low that has passed through the domain. The PV generated by the mountain may affect the downstream development, including the vortices in the wake, and an increase in the PV downstream of the mountain would be a result of increased PV by the mountain. To get an insight into how the PV production varies with nondimensional mountain height, the PV is integrated over a volume of which the horizontal area is shown by a rectangle in Fig. 8 and a gridpoint mean found. In the vertical, most of the PV related to the mountain is concentrated below $\sigma = 0.607$, and the vertical integration is done from the bottom and up to this level. The volume covers the area of the PV banner but avoids taking into account the PV, which is associated with the moving vortices. Figure 9 shows the normalized mean PV, which for constant U increases as $\hat{h}$ increases and there is a relatively good $\hat{h}$ similarity.

b. Idealized flow past Greenland

A simulation was conducted, termed exgreen, with the simple flow described earlier ($U = 10$ m s^{-1}, $N = 0.01$ s^{-1}) but with the idealized mountain replaced by Greenland ($\hat{h} = 3.2$). At a horizontal resolution of 36 km, the topography of Greenland is fairly well represented as shown in Fig. 10. The figure also shows that in the lee of southern Greenland there is a sea level pressure deficit and eddy shedding. Also, as in the more idealized setup there is a wide trough downstream of the mountain at the 500-hPa level. In many ways the flow resembles the flow in ex30 (Fig. 2d), there is no upstream blocking and the vortices are not formed in the vicinity of the tip jet but farther inside the wake (farther north). Nonetheless they are formed farther to

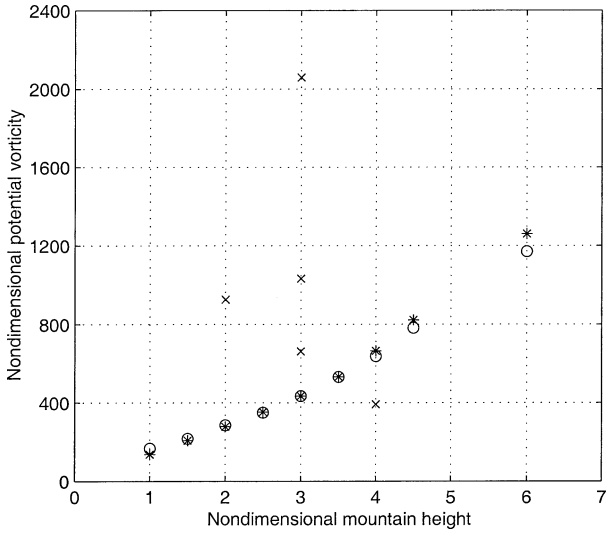

FIG. 9. Nondimensional potential vorticity as a function of $\hat{h}$. The potential vorticity is normalized by $\theta_o N/\rho_o h$, where $\theta_o = 280$ K and $\rho_o = 1.2$ kg m^{-3} are constants. Simulations with $N = 0.01$ s^{-1} and $U = 10$ m s^{-1} (stars), with different combinations of N and h (circles), and where U was varied (crosses) (see Table 1).

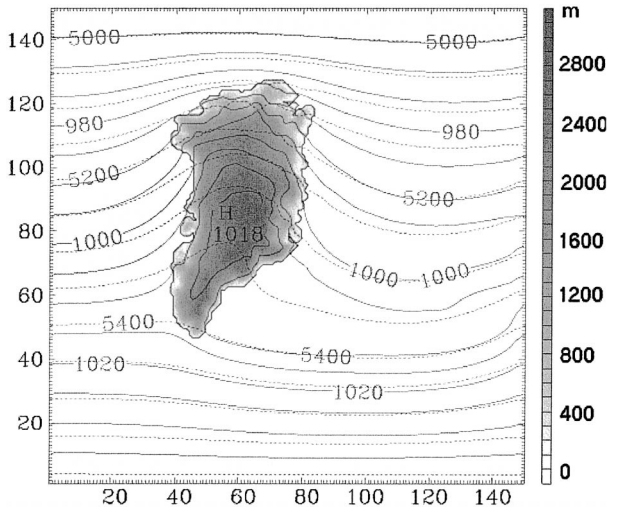

FIG. 10. The sea level pressure (hPa, solid) and geopotential height at the 500-hPa level (m, dashed) in exgreen ($\hat{h} = 3.2$) at $t^* = 47.52$. The orography of Greenland is shaded.

the south of the central part of the mountain than in ex30. The eddy shedding decreases with time. The nondimensional sea level pressure deficit and the nondimensional height deficit at 500 hPa are included in Figs. 5 and 6, respectively. The perturbations for exgreen are only slightly smaller than the ex30 values.

It is interesting to see that even though the simulation is carried out with highly idealized and constant upstream conditions, the resulting sea level pressure field in the lee of the mountain resembles the sea level pressure often seen in reality: The trough closely follows the southeast coast of Greenland and there is a high pressure ridge over Greenland. Apparently, the asymmetry of the mountain and the steepness of the east coast of south Greenland have an impact on the placement of the trough. As the flow is undisturbed far to the south of Greenland, the geopotential deficit in the lee of the mountain at the 500-hPa level results in an enhanced geopotential gradient to the south of the wake. It is particularly interesting to note that the largest gradient and thus the largest westerly wind component (Fig. 7) is far downstream of southern Greenland (Fig. 10). This enhancement of the midtropospheric flow brings us to the next section, where a simulation of a real case illustrates the effect of the Greenland wake on an extratropical cyclone.

5. Real flow over the North Atlantic—A case study

To get a better picture of what impact Greenland's orography can have on the airflow over the North Atlantic, a real case was investigated. The case chosen took place during the Front and Atlantic Storm Track Experiment (FASTEX; Joly et al. 1999) and corresponds to Intensive Observation Period 17 (IOP17) of the experiment, which has been a source of a number of studies (e.g., Cammas et al. 1999). During this period a frontal system, often referred to as the FASTEX cyclone, was triggered off the east coast of the United States, developed and moved eastward. The study includes two simulations, first there is a control simulation and then the same flow is simulated with Greenland's orography set to 1 m, termed nogreen.

a. Model setup

The model setup is the same as used in the idealized simulations, with a few exceptions. The domain is smaller, 135 × 120 grid points, and with its center at 60°N, 30°W it covers the North Atlantic with Greenland as well as a part of the continents on each side. The Burk–Thompson PBL scheme is applied unmodified and the surface roughness is now a function of vegetation. At the top of the model a radiation boundary condition is applied. Since humidity and radiation are included here, the following physical schemes were used: Grell cumulus parameterization, ''simple ice'' explicit condensation scheme and ''cloud-radiation'' scheme (MM5 User's Guide 2001).

The initial and boundary conditions are derived from the European Centre for Medium-Range Weather Forecasts (ECMWF) reanalysis and the lateral boundary conditions are changed every 6 h. In the nogreen simulation, the same ECMWF reanalysis are applied, and the model extrapolates the atmosphere conditions down to sea level over Greenland without creating much noise as can be seen by comparing Figs. 11a and 12a. The simulations were started at 0000 UTC 17 February 1997 and run for 72 h, until 0000 UTC 20 February.

b. The simulations

The evolution of the sea level pressure in the control simulation is shown in Fig. 11. In the initial state there are two developing lows to the east and the southeast of southern Greenland. The northern low moves to the west and becomes quasi-stationary just east of southern Greenland. The southern low moves northeast and later north, and after 48 h of simulation it has become a trough northeast of the quasi-stationary low. After 20 h of simulation the FASTEX cyclone enters the domain south of Newfoundland and moves east and later northeast. At the end of the simulation the cyclone is stationed between Scotland and the Shetland Islands and is starting to fill.

Figure 12 shows the evolution of the sea level pressure in the nogreen simulation. In the absence of Greenland's orography, there is no quasi-stationary low in the area just east of southern Greenland. In fact after 48 h of simulation, there is a high pressure ridge in this area, while at the end of the simulation a low has moved into the area from west. During the last 21 h of simulation, the FASTEX cyclone passing far south of Greenland, moves slower (Figs. 11d and 12d) and is shallower than

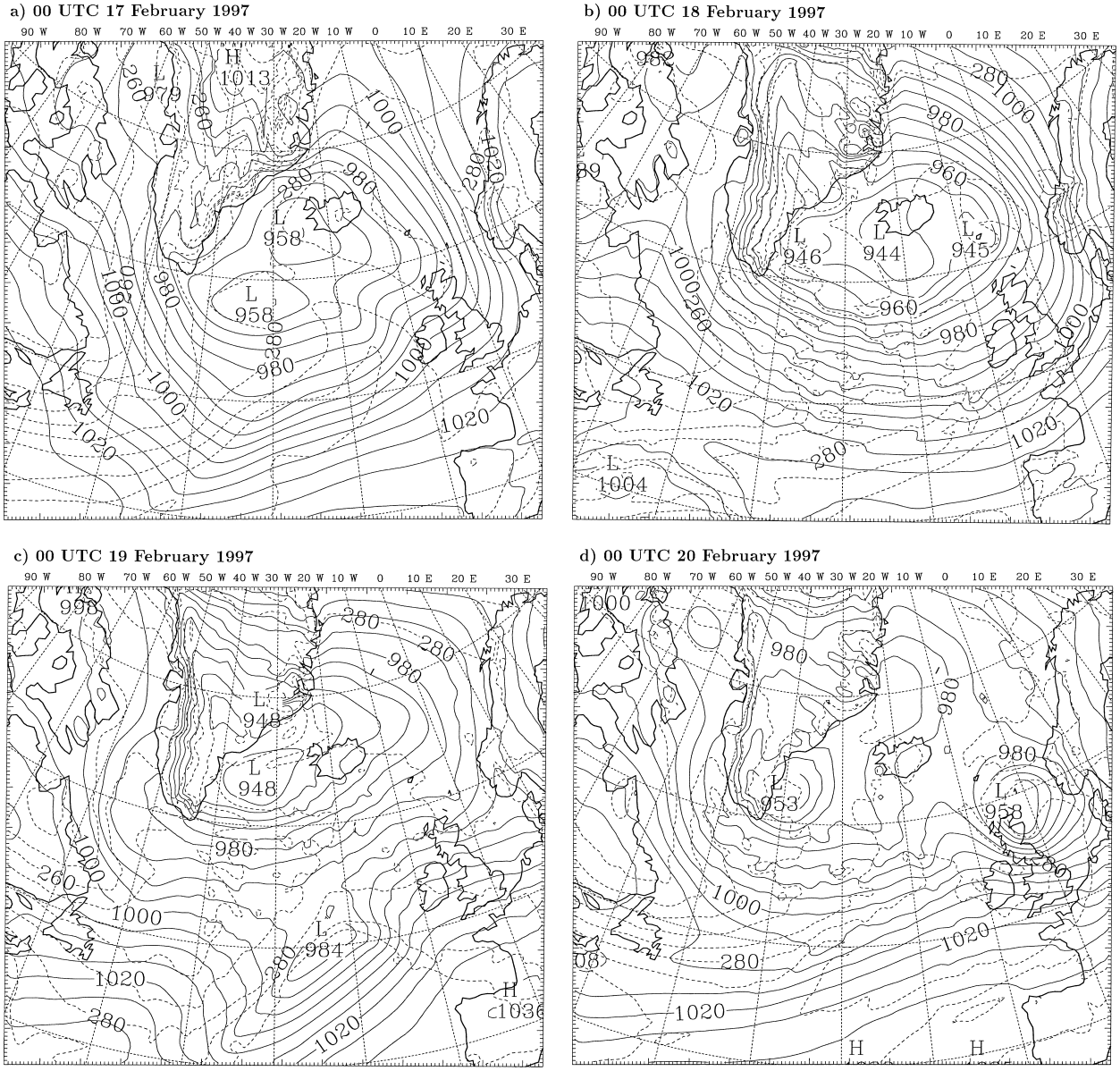

FIG. 11. Sea level pressure (hPa, solid) and potential temperature (K, dashed) at 850 hPa in the control simulation: (a) 0 h, valid 0000 UTC 17 Feb; (b) 24 h, valid 0000 UTC 18 Feb; (c) 48 h, valid 0000 UTC 19 Feb; and (d) 72 h, valid 0000 UTC 20 Feb 1997.

in the control simulation (Fig. 13). Note also the weaker thermal gradient behind the cyclone in the nogreen simulations (Fig. 12d) in comparison with the control simulation (Fig. 11d), that could contribute to weaker cyclogenesis.

In the control simulation the quasi-stationary low in the lee of Greenland reaches up to the 500-hPa level (Fig. 14a), increasing the gradient in the geopotential height to the southeast of Greenland. In contrast, in the absence of Greenland's orography, and thus the quasi-stationary surface low, there is no low at the 500-hPa level, resulting in a weaker gradient in the 500-hPa level southeast of Greenland; see Fig. 14b.

These differences result in different propagation speed and depth of the FASTEX cyclone after it has reached the flow field influenced by Greenland's orography.

6. Discussion and conclusions

The flow in the idealized simulations carried out in this study can be divided into three classes: (a) for low $\hat{h}$ the flow is unblocked and quasi-stationary, (b) for intermediate $\hat{h}$ the flow is unblocked but with diminishing eddy shedding in the lee and is striving towards quasi stationarity, and (c) for high $\hat{h}$ the flow is blocked

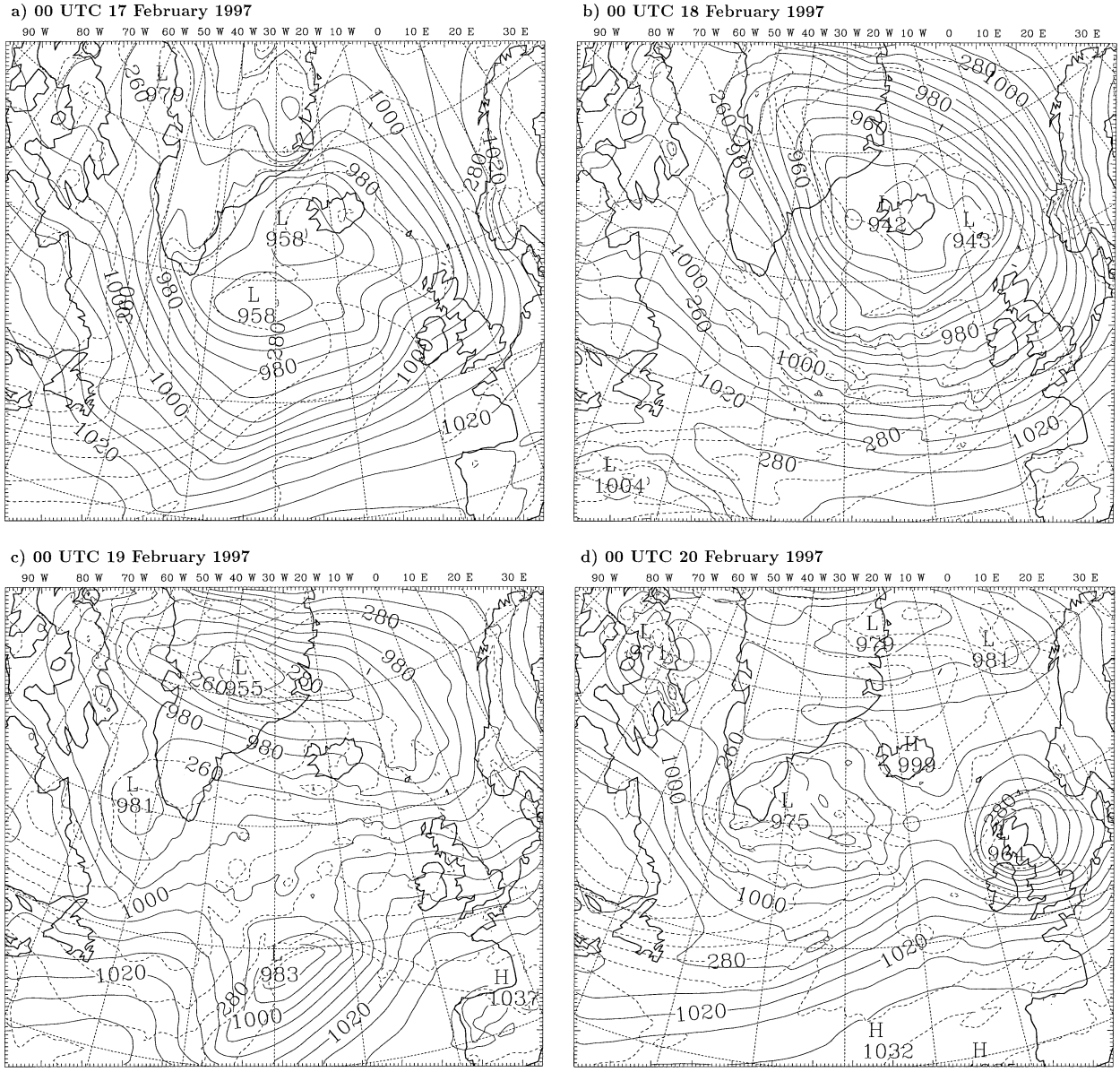

FIG. 12. Sea level pressure (hPa, solid) and potential temperature (K, dashed) at 850 hPa in the nogreen simulation: (a) 0 h, valid 0000 UTC 17 Feb; (b) 24 h, valid 0000 UTC 18 Feb; (c) 48 h, valid 0000 UTC 19 Feb; and (d) 72 h, valid 0000 UTC 20 Feb 1997.

with continuous eddy shedding in the lee of the mountain. According to Smith (1989), it is with the onset of upstream blocking and thus flow splitting, that complex shear layer and vortex structures begin to appear in the wake. In our simulations, vortex structures are also found in the wake of the mountain in some unblocked cases, but unlike in the blocked regime, the activity decreases with time.

Three nondimensional diagnostic parameters were calculated, that is, maximum sea level pressure deficit, maximum geopotential height deficit at the 500-hPa level, both in the wake, and low-level PV integrated over a finite volume covering the shear line between the flow in the lee and the tip jet. For constant upstream wind speed, the simulated flows show good $\hat{h}$ similarity, but with variations in U the similarity seems to break down at least for the 500-hPa geopotential deficit and the PV downstream of the mountain. The failure of the similarity of the PV must be related to the internal dissipation, which is not included in the theory on which the similarity of orographic flows is based (e.g., Smith and Grønås 1993). Such a dissipation is a necessary condition for the generation of PV in our free-slip flows. In balanced flows, the geopotential is linked to the PV and the lack of similarity in the geopotential is consequently not unexpected.

The nondimensional parameters show that, for a constant upstream wind speed, $\hat{h}$ increases, as the pressure

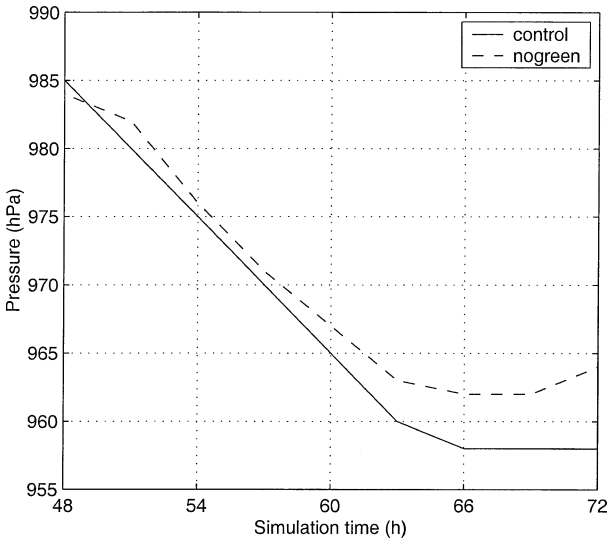

FIG. 13. The sea level pressure (hPa) in the center of the FASTEX cyclone in the control simulation (solid) and the nogreen simulation (dashed).

deficit increases both at sea level and at midtropospheric levels. That is also the case for the mean PV. There are no abrupt changes in the parameters calculated at the regime shift between unblocked and blocked flow, the increase is gradual and smooth, but with the largest gradient at the regime shift. It seems likely that the low Rossby number applied here, Ro = 0.42, has this effect of smoothing the transition between the flow regimes. This kind of smoothing has been suggested by Thorpe et al. (1993).

For constant U the PV production by the mountain increases with increasing $\hat{h}$, while the area of wave breaking moves farther north. The PV is generated by the mountain through internal dissipation and diffusion. Even though the airflow is complex due to the Coriolis force, the results of Rotunno et al. (1999) and Epifanio and Durran (2002) should apply here. The PV produced by the mountain accumulates in the vortices shedding downstream (Fig. 8) and has impact on the geopotential height, causing a geopotential height deficit at the 500-hPa level far from the mountain. This height deficit results in a stronger gradient in geopotential height south of the lee area as can be detected by increasing wind speed in this region (Fig. 7).

The idealized simulations are capable of shedding a new light on the development of a cyclone over the North Atlantic. Through the production of PV, a larger mountain results in a large surface pressure deficit downstream and a larger deficit in the geopotential at the 500-hPa level. The latter results in a stronger gradient in the geopotential to the south of the lee area, which has a positive impact on cyclone development moving far south of the mountain as is the case of the FASTEX cyclone.

These results have important implications for the interpretation of GCM simulations. A coarse resolution model, representing Greenland poorly, may give large prediction errors, not only confined to the area just east of Greenland but in a more extensive area south of the mountain wake. Poor resolution of Greenland can thus affect the prediction of storm tracks and can result in underestimations of the speed and depth of cyclones moving far south of Greenland towards northwest and central Europe.

The present study has raised a number of questions,

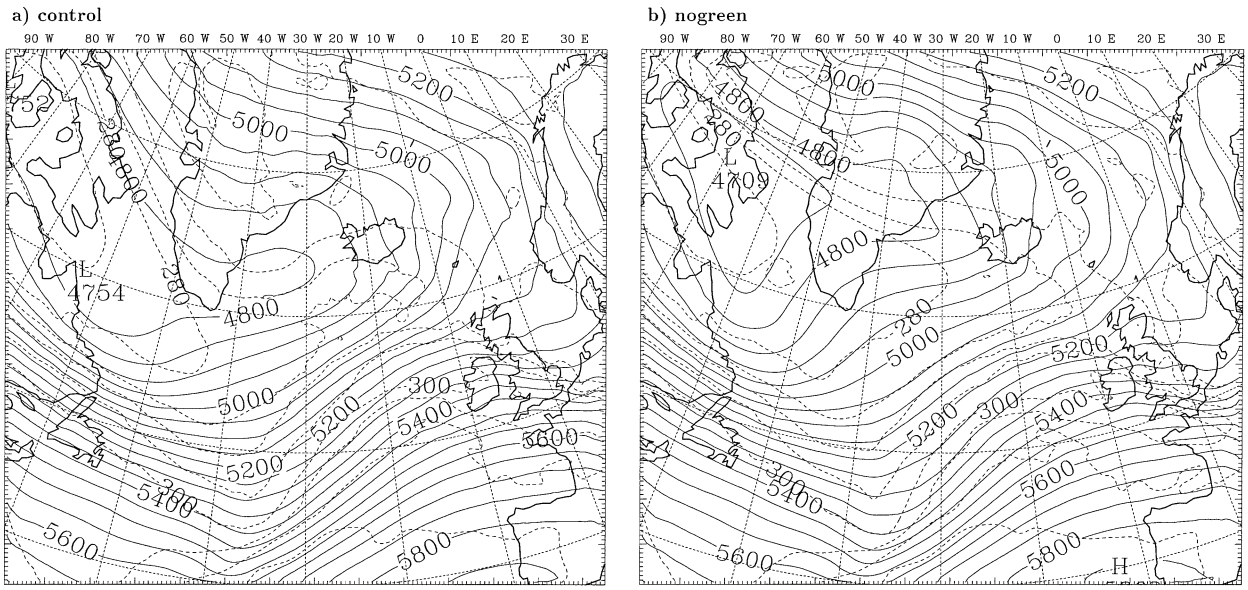

FIG. 14. The 500-hPa geopotential height (m, solid) and potential temperature (K, dashed) in (a) the control and (b) the nogreen simulation after 48 h of simulation, valid 0000 UTC 19 Feb 1997.

for example, regarding the similarity of complex mountain flow and the effect of the surface friction on the flow. These problems will undoubtedly be objects of future research in the field of interaction between orography and the atmosphere.

Acknowledgments. This research is partly financed by the Research Council of Norway (Grant 133634/432) and the EU project FASTEX-CSS. Furthermore, the authors would like to thank Ronald B. Smith and Sigbjørn Grønås for valuable discussions during the research and Dr. Dough Parker and one anonymous reviewer for valuable comments and suggestions.

REFERENCES

Aebischer, U., and C. Schär, 1998: Low-level PV and cyclogenesis to the lee of the Alps. *J. Atmos. Sci.,* **55,** 186–207.

Bougeault, P., B. Benech, P. Bessemoulin, B. Carissimo, A. Jansa Clar, J. Pelon, M. Petitdidier, and E. Richard, 1997: PYREX: A summary of findings. *Bull. Amer. Meteor. Soc.,* **78,** 637–650.

Breivik, L.-A., J. E. Kristjánsson, K. H. Midtbø, B. Røsting, and J. Sunde, 1992: Simulations of the 1 January 1992 North Atlantic storm. The Norwegian Meteorological Institute Tech. Rep. 99, 69 pp.

Burk, S. D., and W. T. Thompson, 1989: A vertically nested regional numerical weather prediction model with second-order closure physics. *Mon. Wea. Rev.,* **117,** 2305–2324.

Cammas, J.-P., and Coauthors, 1999: FASTEX IOP17 cyclone: Introductory synoptic study with field data. *Quart. J. Roy. Meteor. Soc.,* **125,** 3393–3414.

Davis, C., 1997: The modification of baroclinic waves by the Rocky Mountains. *J. Atmos. Sci.,* **54,** 848–868.

Doyle, J. D., and M. A. Shapiro, 1999: Flow response to large-scale topography: The Greenland tip jet. *Tellus,* **51A,** 728–748.

Durran, D. R., 1990: Mountain waves and downslope winds. *Atmospheric Processes over Complex Terrain, Meteor. Monogr.,* No. 45, Amer. Meteor. Soc., 59–81.

Eliassen, A., and E. Palm, 1960: On the transfer of energy in stationary mountain waves. *Geophys. Norv.,* **22,** 1–23.

Epifanio, C. C., and D. R. Durran, 2001: Three-dimensional effects in high-drag-state flows over long ridges. *J. Atmos. Sci.,* **58,** 1051–1065.

——, and ——, 2002: Lee-vortex formation in free-slip stratified flow over ridges. Part II: Mechanisms of vorticity and PV production in nonlinear viscous wakes. *J. Atmos. Sci.,* **59,** 1166–1180.

Grell, G. A., J. Dudhia, and D. R. Stauffer, 1995: A description of the fifth-generation Penn State/NCAR mesoscale model (MM5). NCAR Tech. Note NCAR/TN-398 + STR, 122 pp.

Grønås, S., 1995: The seclusion intensification of the New-Year's-day storm 1992. *Tellus,* **47A,** 733–746.

Grubišić, V., R. B. Smith, and C. Schär, 1995: The effect of bottom friction on shallow-water flow past an isolated obstacle. *J. Atmos. Sci.,* **52,** 1985–2005.

Harold, J. M., G. R. Bigg, and J. Turner, 1999a: Mesocyclone activity over the Northeast Atlantic. Part 1: Vortex distribution and variability. *Int. J. Climatol.,* **19,** 1187–1204.

——, ——, and ——, 1999b: Mesocyclone activity over the Northeast Atlantic. Part 2: An investigation of causal mechanisms. *Int. J. Climatol.,* **19,** 1283–1299.

Held, I. M., 1983: Stationary and quasi-stationary eddies in the extratropical troposphere: Theory. *Large-Scale Dynamical Processes in the Atmosphere,* B. J. Hoskins and R. P. Pearce, Eds., Academic Press, 127–168.

Joly, A., and Coauthors, 1999: Overview of the field phase of the Front and Atlantic Storm-Track EXperiment (FASTEX) project. *Quart. J. Roy. Meteor. Soc.,* **125,** 3131–3163.

Klemp, J. B., and D. K. Lilly, 1978: Numerical simulation of hydrostatic mountain waves. *J. Atmos. Sci.,* **35,** 78–107.

Kristjánsson, J. E., and H. McInnes, 1999: The impact of Greenland on cyclone evolution in the North Atlantic. *Quart. J. Roy. Meteor. Soc.,* **125,** 2819–2834.

Mellor, G. L., and T. Yamada, 1982: Development of a turbulence closure model for geophysical fluid problems. *Rev. Geophys. Space Phys.,* **20,** 851–875.

MM5 User's Guide, 2001: PSU/NCAR Mesoscale Modeling System, Tutorial Class Notes and User's Guide: MM5 Modeling System Version 3. PSU/NCAR, 300 pp.

Ólafsson, H., 1998: Different prediction of two NWP models of the surface pressure NE of Iceland. *Meteor. Appl.,* **5,** 253–261.

——, 2000: How do mountains reduce windspeed? (in French). *La Météorologie,* **8,** 19–24.

——, and P. Bougeault, 1996: Nonlinear flow past an elliptic mountain ridge. *J. Atmos. Sci.,* **53,** 2465–2489.

——, and ——, 1997: The effect of rotation and surface friction on orographic drag. *J. Atmos. Sci.,* **54,** 193–209.

Pierrehumbert, R. T., and B. Wyman, 1985: Upstream effects of mesoscale mountains. *J. Atmos. Sci.,* **42,** 977–1003.

Queney, P., 1948: The problem of the airflow over mountains: A summary of theoretical studies. *Bull. Amer. Meteor. Soc.,* **29,** 16–26.

Rotunno, R., V. Grubišić, and P. K. Smolarkievicz, 1999: Vorticity and potential vorticity in mountain wakes. *J. Atmos. Sci.,* **56,** 2796–2810.

Schär, C., 1993: Notes and correspondence: A generalization of Bernoulli's theorem. *J. Atmos. Sci.,* **50,** 1437–1443.

——, and R. B. Smith, 1993: Shallow-water flow past isolated topography. Part I: Vorticity production and wake formation. *J. Atmos. Sci.,* **50,** 1373–1400.

——, and D. R. Durran, 1997: Vortex formation and vortex shedding in continuously stratified flows past isolated topography. *J. Atmos. Sci.,* **54,** 534–554.

Smith, R. B., 1989: Hydrostatic airflow over mountains. *Advances in Geophysics,* Vol. 31, Academic Press, 59–81.

——, and S. Grønås, 1993: Stagnation points and bifurcation in 3-D mountain airflow. *Tellus,* **45A,** 28–43.

——, A. C. Gleason, P. A. Gluhosky, and V. Grubišić, 1997: The wake of St. Vincent. *J. Atmos. Sci.,* **54,** 606–623.

Smolarkiewicz, P. K., and R. Rotunno, 1989: Low Froude number flow past three-dimensional obstacles. Part I: Baroclinically generated lee waves. *J. Atmos. Sci.,* **46,** 1154–1164.

——, and ——, 1990: Low Froude number flow past three-dimensional obstacles. Part II: Upwind flow reversal zone. *J. Atmos. Sci.,* **47,** 1498–1511.

Steenburgh, W. J., and C. F. Mass, 1994: The structure and evolution of a simulated Rocky Mountain lee trough. *Mon. Wea. Rev.,* **122,** 2740–2761.

Thorpe, A. J., H. Volkert, and D. Heimann, 1993: Potential vorticity of flow along the Alps. *J. Atmos. Sci.,* **50,** 1573–1590.

Thorsteinsson, S., and S. Sigurðsson, 1996: Orogenic blocking and deflection of stratified air flow on an f-plane. *Tellus,* **48A,** 572–583.